AIAA SciTech Forum
23-27 January 2023, National Harbor, MD & Online
AIAA SCITECH 2023 Forum

10.2514/6.2023-0465

Spatially Distributed Measurements of Ejecta Concentrations in Plume-Surface Interactions using Millimeter Wave Interferometry

Nicolas Rasmont[1], Hussein T. Al-Rashdan[2], Gregory S. Elliott[3], Joshua L. Rovey[4], and Laura Villafañe[5]
University of Illinois at Urbana-Champaign, Urbana IL, 61801

Millimeter-wave interferometry has shown much promise to measure particle concentrations in opaque, dispersed multiphase flows such as those encountered in plume-surface interactions. This study expands on a previously developed proof-of-concept millimeter-wave interferometer, demonstrating several mission-critical capabilities and providing unique insights in the ejecta dynamics of plume-surface interactions. An innovative vacuum calibration procedure reduced measurement uncertainties by one order of magnitude compared to prior calibrations at ambient conditions thanks to the reduction of aerodynamic entrainment. Calibration experiments verified the theoretical linear relation between phase shift and path-integrated particle number density and provided the constant proportionality factor for the specific glass microspheres and radar system employed. The instrument was demonstrated on a reduced-scale plume-surface interaction experiment. Ejecta path-integrated concentrations were measured at two ambient pressure levels representative of Lunar (14.26 Pa) and Martian (800 Pa) surface conditions, confirming the trends observed during prior experiments. Further experiments were conducted at 800 Pa to demonstrate the capability of the instrument to operate in very close proximity to the ground, and to analyze the distribution of ejecta with altitude. Ejecta path-integrated concentrations measured at 9, 6, and 3 cm above the granular surface provided maximum values of $(1.284 \pm 0.040) \times 10^9$ #.m^{-2}, $(2.345 \pm 0.051) \times 10^9$ #.m^{-2}, and $(6.881 \pm 1.659) \times 10^9$ #.m^{-2} respectively. Ongoing developments of millimeter-wave interferometry for concentration measurements aim at providing the 3D spatial distribution of ejecta cloud concentrations. To that end, a preliminary demonstration of 3D tomographic capabilities was performed using 3 reflectors, each defining a distinct measurement path. A tomographic reconstruction algorithm was implemented to convert path-integrated concentrations into standard concentrations, providing a maximum of $(10.140 \pm 0.442) \times 10^9$ #.m^{-3} measured at a radial distance of 8.8 cm from the nozzle axis.

I. Nomenclature

β_n	=	Slope of the calibration curve between measured phase shift and path-integrated number concentration
c_0	=	Speed of light in vacuum
D	=	Nozzle exit diameter
$\bar{D_p}$	=	Average particle diameter
δ_p	=	Particle volume fraction
$\Delta\phi$	=	Measured phase shift
ε_p	=	Dielectric constant of the particles
ε_m	=	Dielectric constant of the medium (air/vacuum)
f_0	=	Radar operating frequency
h	=	Height over the granular bed (measurement path or nozzle exit plane)
$l_{i,j}$	=	Length of path i intersecting region j

[1]PhD Candidate, Department of Aerospace Engineering, 324 Talbot Laboratory, 104 South Wright St, AIAA Student member.
[2]PhD Candidate, Department of Aerospace Engineering, 324 Talbot Laboratory, 104 South Wright St, AIAA Student Member.
[3]Professor, Department of Aerospace Engineering, 301 Talbot Laboratory, 104 South Wright St, AIAA Associate Fellow.
[4]Associate Professor, Department of Aerospace Engineering, 317 Talbot Laboratory, 104 South Wright St, AIAA Associate Fellow.
[5]Assistant Professor, Department of Aerospace Engineering, 313 Talbot Laboratory, 104 South Wright St, AIAA Member.

n = Number of open slots during calibration
n_k = Number concentration of reconstruction layer k
n_p = Particle number concentration
p_e = Static pressure at nozzle exit
p_i = Path-integrated number concentration of measurement path i
p_∞ = Ambient pressure
PSI = Plume-Surface Interactions
r_g^2 = Coefficient of determination
$\mathbf{W}$ = Reconstruction weight matrix

II. Introduction

When a spacecraft performs a rocket-powered landing on a planetary surface, the interactions between the exhaust plume of the thruster and the surface material give rise to a set of complex physical phenomena grouped under the name of Plume-Surface Interactions (PSI). PSI are a significant concern for current and future exploration missions to the Moon and Mars [1, 2], as they are associated with a number of mission-critical hazards represented in Fig. 1: unpredicted aerodynamic stresses [3], the formation of a transient crater capable of burying or toppling the spacecraft [4, 5], and the generation of a dust cloud capable of blinding guidance instruments and damaging the spacecraft and nearby ground systems [6–8]. Improving the scientific understanding of PSI is an important component of NASA's research goals [9], with potentially far-reaching consequences for the return of humans on the Moon planned within the next decade by the Artemis program.

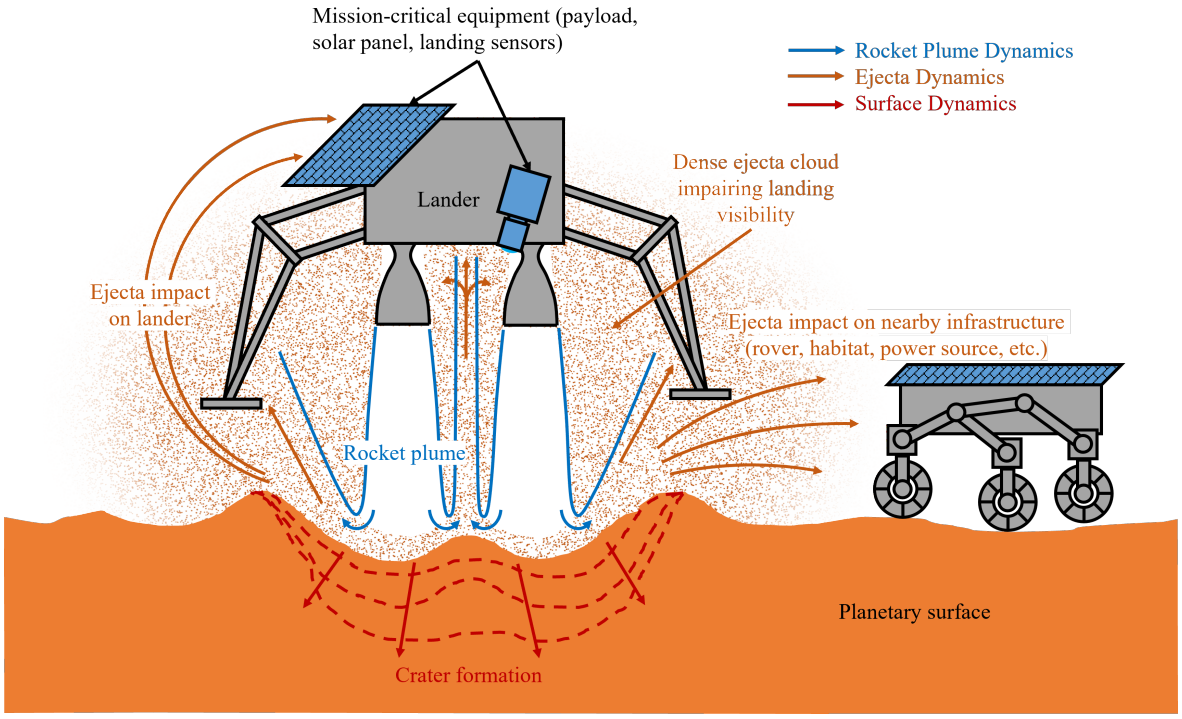

Fig. 1 Diagram representing the physics and hazards associated with Plume-Surface Interactions.

The current corpus of experimental data relevant to PSI is insufficient to support the development of high-fidelity models (theoretical and numerical) needed to inform the design of future planetary missions. In-situ observations acquired by flight instruments are restricted to footage and photographs acquired by the Apollo missions[7], Perserverance and Curiosity rovers [10], and Chang'E-4 probe [11]. New instruments, such as the Stereo Cameras for Lunar Plume Surface Studies (SCALPSS) [12] capable of monitoring crater formation during landing, are being deployed through NASA's Commercial Lunar Payload Service (CLPS). On the other hand, PSI ground tests are challenged by a range of operational and physical difficulties. The requirement to maintain a pressure relevant to the Martian or Lunar surface

is in direct conflict with the presence of a jet injecting large quantities of gas in the chamber, far above the pumping speed of existing vacuum systems. Consequently, when conducting a PSI experiment, even very large vacuum facilities are capable of maintaining an acceptable ambient pressure for only a few seconds [13, 14]. The presence of invasive dust in the vacuum chamber can compromise seals, diagnostics, and pumping systems. Finally, the large quantities of opaque ejecta generated by PSI prevent, in most cases, the use of optical diagnostics to measure particle and fluid phase properties. Most PSI experiments reported in the literature [4, 5, 14–18] alleviate this issue by dividing the experiment space in two, using a splitter plate. This method allows direct optical access to the jet and underlying crater at the cost of altering the 3D axisymmetric nature of the problem. This has led to a growing interest in non-intrusive PSI diagnostic techniques capable of operating without a splitter plate. Such diagnostics would be applicable to ground experiments and flight instruments. Quantitative measurements of particle concentrations, in particular, are of high interest [19]. In earlier research, Lane and Metzger used optical methods to determine the number density of a Lunar landing ejecta cloud by measuring optical extinction[20, 21] and particle side-scattering [22]. Optical transmission rapidly falls to zero for number concentrations higher than 10^{10} #.m^{-3} and particle diameters larger than 10 μm, which restricts optical techniques to the measurement of low concentrations of small particles. In addition, optical methods are quite imprecise, resulting in margins of error spanning six orders of magnitude in one instance [7].

A novel method capable of accurately measuring the concentrations of dense ejecta clouds has been demonstrated by the authors [23]. It is based on the principle of millimeter-wave (mmWave) radar interferometry, using a frequency-modulated, continuous-wave radar system capable of measuring the path-integrated concentration of suspended particles with a repetition rate of 20 kHz, independently of the size distribution of the material, for a range of concentrations at least one order of magnitude higher than optical techniques. In this work, we present the progress that has been accomplished in the development of this instrument. A novel vacuum calibration technique has improved the precision of our measurements by one order of magnitude over the previous calibrations performed at ambient conditions. Significant improvements have been made in the acquisition frequency and noise figure of our instrument. A campaign of spatially distributed measurements has been performed across several measurement altitudes and azimuth angles, improving our understanding of the time-resolved spatial distribution of the ejecta cloud. In particular, azimuth-distributed measurements are used to demonstrate the tomographic capability of our instrument.

III. Experimental methods

A. Millimeter-wave radar interferometer

When a mmWave beam travels between a transmitter TX and a receiver RX, particles present along the propagation path slows down the phase velocity of the waves. This leads to a phase shift $\Delta\phi$ on the received signal that is proportional to the particle volume fraction integrated along the propagation path $\int_{\mathrm{TX}}^{\mathrm{RX}} \delta_p dl$, according to Eq. 1 [23, 24]:

$$\Delta\phi = \frac{3\pi f_0}{c_0}\left(\frac{\varepsilon_p - \varepsilon_m}{\varepsilon_p + 2\varepsilon_m}\right)\int_{\mathrm{TX}}^{\mathrm{RX}} \delta_p dl \tag{1}$$

The phase shift $\Delta\phi$ can be measured using an interferometer. This method has two key benefits. First, micrometer to millimeter-sized particles have a low extinction efficiency in the mmWave range (four orders of magnitudes lower than visible light), which allows concentration measurements of dense, opaque ejecta clouds, such as those encountered in PSI experiments. Secondly, $\Delta\phi$ provides a direct measurement of the volume fraction of the particles, independently of the particle size distribution. This is an improvement over optical particle concentration measurement systems, which usually require the size distribution to be known or measured in advance. This concept is implemented using a phase-coherent frequency-modulated continuous wave (FMCW) radar associated with one or several reflectors defining fixed-length measurement paths, shown in Fig. 2. The radar generates a mmWave beam and measures the phase of the signal reflected by the reflector, providing the particle concentration integrated along the propagation path.

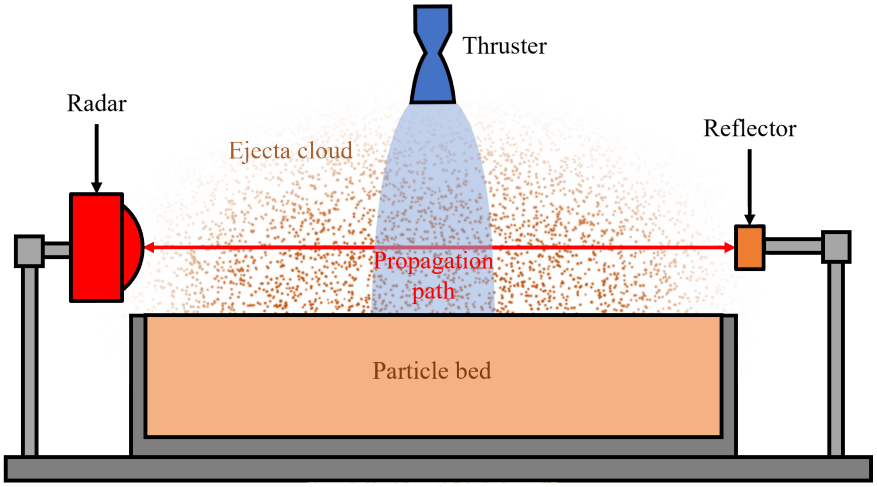

Fig. 2 Diagram of the mmWave radar interferometer in its experimental configuration.

The radar system includes two IWR1443BOOST and DCA1000EVM evaluation boards manufactured by Texas Instruments. The AWR144BOOST carries a IWR1443 [25] 77-81 GHz FMCW radar chip, while the DCA1000EVM [26] captures raw ADC data from the radar and streams it to a computer over a 1 GBps Ethernet link. This new system has two advantages over the radar system used previously by the authors for the proof-of-concept experiments reported in [23]. First, the acquisition rate of the system has been increased from 10 kHz to 20 kHz by eliminating an impedance mismatch in our ethernet line and discarding irrelevant range data prior to transmission. Secondly, the IWR1443 radar data displays a vastly reduced in-phase/quadrature (IQ) imbalance compared to the IWR6843, leading to a lower noise figure. The measurement paths are defined using 31.75 mm diameter copper disk reflectors. Planar reflectors are used instead of more conventional corner cubes because of their highly directional cross-section, which reduces the effect of multipath interference. The boards are protected from the ejectas by an enclosure integrating a cylindrical Fresnel zone plate [27] dielectric lens made of PTFE to improve beam collimation.

B. Calibration Method

The objective of the calibration procedure is to establish the relationship between the phase shift measured by the instrument and the actual path-integrated concentration. A significant challenge to calibrating our instrument is the generation of a high particle concentration calibration standard characterized in an independent, repeatable, and reliable way. Trusted optical measurement systems cannot reach the high concentration range covered by our instrument. A divide-and-conquer approach capable of solving this problem was developed and demonstrated by the authors [23]. First, a funnel with 25 individually addressable slots is used to generate thin sheets of falling particles. The path-integrated concentration of each sheet is low enough to be measured by a backilluminated, high-resolution, optical particle-counting system, as shown in Fig. 3. Once each sheet has been independently characterized, it is possible to generate a particle cloud with a known path-integrated concentration by opening multiple slots. By reporting the phase shift measured by the radar for a given number of open slots, a calibration curve covering all or a significant fraction of the measurement range can be established. The current study improves significantly on prior work by conducting the calibration process under reduced atmospheric pressure ($\approx$ 300 Pa). This eliminates aerodynamic effects such as gas-particle entrainment and turbulence, which introduced large errors in the calibration curve ; the path-integrated concentration generated by n open slots could not be assumed to be n times that of a single slot. The reduced-pressure calibration takes place in the same vacuum facility used for PSI experiments. A piston actuator is used to remotely trigger the slot funnel.

Because the instrument is calibrated against an optical technique providing path-integrated number concentrations, the results in the next sections will be reported as $\#.m^{-2}$. Volume concentrations δ_p can be obtained from number concentrations n_p and mean particle diameter $\bar{D_p}$ using Eq. 2. This procedure is applicable both for path-integrated and local quantities.

$$\delta_p = \frac{\pi}{6} \bar{D_p}^3 n_p \tag{2}$$

Uncertainty on the particle size distribution translates on larger uncertainties on volumetric concentrations when

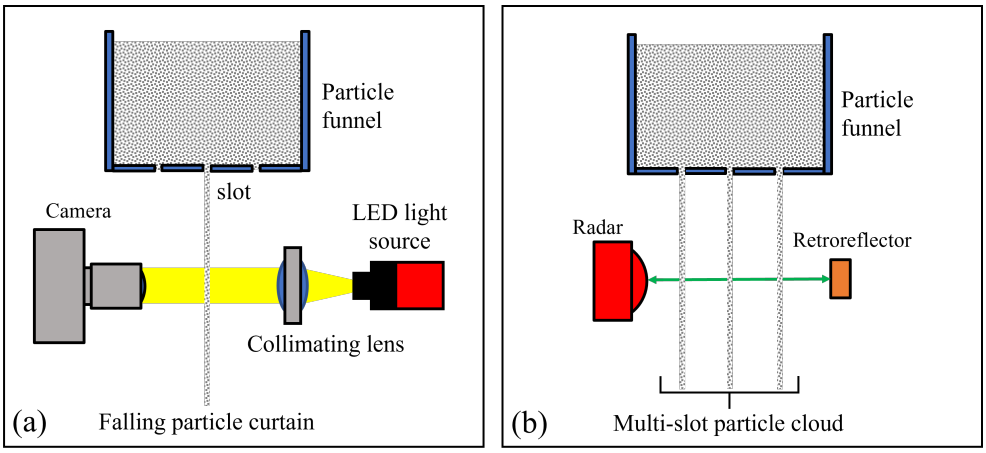

Fig. 3 Concept diagram for the optical step (a), and radar step (b) of the calibration process.

compared to number concentrations. This is a consequence of the optical calibration method used and not the measurement principle. Future work is needed to develop reduced or optic-independent calibration techniques capable of deriving the phase-to-volume-fraction coefficient of the instrument without having to use an optical number concentration measurement as a point of reference.

C. Plume-Surface Experiment

The experiments are conducted in the PSI vacuum facility of the Electric Propulsion Laboratory at the University of Illinois at Urbana-Champaign (UIUC) described [23, 28]. The chamber is 1.2 m in diameter and 2.1 m long for a total volume of 2375 liters. It is capable of a base pressure of 1 Pa. A 30.5 cm-tall, 61 cm-wide cylindrical PVC bed contains the granular material, shown in Fig. 4. A 6.5N cold gas thruster generates a 8.6 g/s nitrogen jet with a nozzle exit velocity of Mach 5 that impinges on the granular surface. It is fed from a pressurized reservoir at 1.227 MPa and ambient temperature (295 K). A high-speed solenoid valve remains fully open during 1 second, the chosen test duration. It is important to notice that the ratio between the static pressure of the jet at the nozzle exit plane and the ambient chamber pressure p_e/p_∞ decreases during the course of the experiment, due to limited pumping speed and chamber volume relative to the mass flow rate of the jet. At 800 Pa, p_e/p_∞ decreases from 2.85 to 2.46 (moderately underexpanded jet); at 14.26 Pa, from 160 to 13.4 (highly underexpanded jet). The height of the thruster above the surface is controlled by a linear stage; it was set at 15 cm for this study, which corresponds to a ratio of height to nozzle diameter (h/D) of 15.

Fig. 4 Details of the PSI facility showing the cold gas thruster (1) and granular media bed (2).

Three experimental configurations are studied for a total of five measurements. First, the effect of ambient pressure

is measured by comparing path-integrated concentrations at 14.26 Pa (referred to in the following as Lunar conditions) and 800 Pa (Martian conditions). The 58cm-long measurement path is perpendicular with the nozzle axis and 9 cm (9 h/D) above the surface. The second test case aims at studying the distribution of particles as a function of height above the granular surface. Three experiments with measurement path heights 9, 6, and 3 cm (9, 6, and 3 h/D), shown in Fig. 5, are conducted at an ambient pressure of 800 Pa. The measurement paths are likewise 58-cm long and perpendicular with the nozzle axis. Finally, a demonstration of the tomographic capabilities of the instrument is conducted using 3 measurement paths with respective azimuth angles of 0°, 8.4°, and 16.8°, lengths of 58.5, 68.5, and 80.5 cm, all at a constant altitude of 9 h/D above the surface. Those three measurement paths, shown in Fig. 5, are realized using three reflectors staggered at various ranges. This allows the radar to separate the signal associated with each path, as shown in the range data presented in Fig. 6.

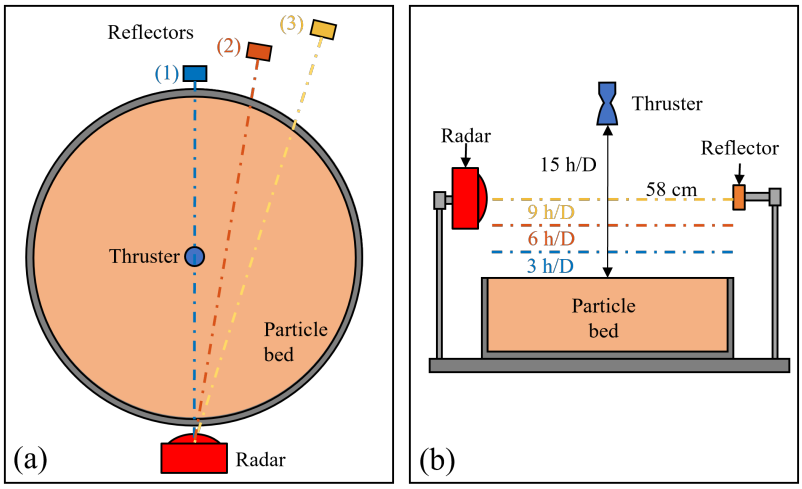

Fig. 5 Diagram of measurement paths in tomographic (a) and in varying height configuration (b).

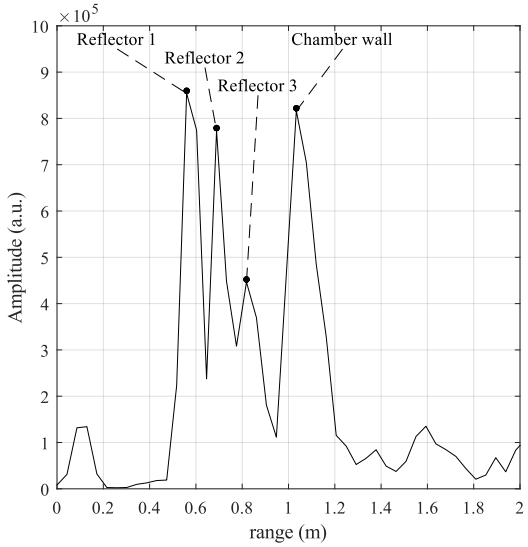

Fig. 6 Tomographic range diagram, showing the peaks corresponding to reflectors and chamber wall.

D. Granular Material

The particles used as regolith simulant are Ballotini solid glass microspheres with a density $\rho = 2500$ kg.m^{-3}. The particle size distribution was determined using X-ray microtomography (micro-CT) images obtained with an Xradia MicroXCT-400. The tomographic images are segmented using a watershed algorithm, resulting in a set of individually labelled and sized particles from which the size distribution of the sample can be deduced. This measurement is validated by sieving, using a dry sieve shaker with size breaks at 53, 63, 90, 106, 125, 150, 180, 250, and 350 μm. The results of both measurements are reported in Fig. 7 and Table 1. We observe a close agreement between the mean diameters of the micro-CT distribution and the sieving distribution, with less than 1% difference between the two values. The median, 5th percentile, and 95th percentiles are also within 5% of each other. The larger gap observed for the mode diameter can be explained by the lower resolution of the sieving distribution. The mode is the center of the most populated bin, even if the actual population within the bin is skewed toward lower or higher values.

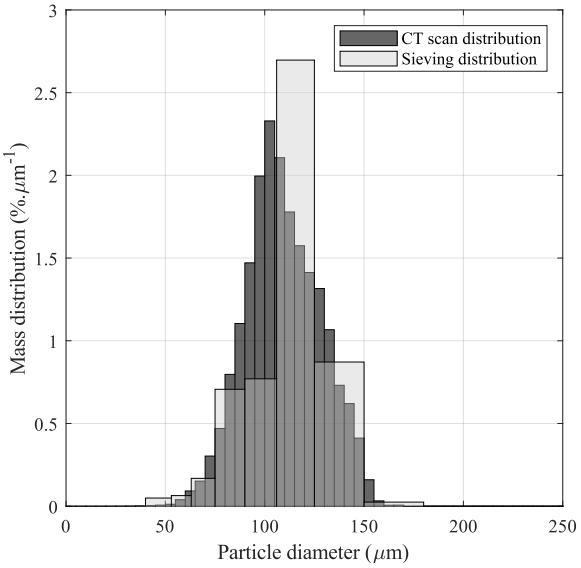

Fig. 7 Comparison between the particle size-mass distribution measured by micro-CT scanning and sieving.

Table 1 Mass distribution properties obtained through micro-CT scanning, and sieving.

Parameter (μm)	Micro-CT	Sieving
Error	6.7	9.7
Mean	109.2	110.1
Median	107.8	113.0
Mode	102.5	115.5
5th percentile	79.2	75.8
95th percentile	141.8	138.1

E. Tomographic reconstruction

A tomographic reconstruction is performed to extract the spatial distribution of ejecta from the multi-azimuth test. Given that three coplanar measurement paths are used, the reconstruction provides a distribution of the particles within the plane. The distribution is assumed to be axisymmetric around the nozzle axis. First, the test area is discretized in a set of k concentric regions with uniform concentration $n_1, ..., n_k$. The path-integrated concentration p_i of measurement path i is defined by Eq. 3:

$$p_i = \sum_{j=1}^{k} l_{i,j} n_j \tag{3}$$

With $l_{i,j}$ the length of path i intersecting region j. In matrix form, with $\boldsymbol{W}$ the weight matrix containing the $l_{i,j}$ the problem becomes:

$$p = \boldsymbol{W} \cdot n \tag{4}$$

The concentration of each layer is then determined from the solution $\hat{n}$ of the following linear program:

$$\text{minimize} \quad \|\boldsymbol{W} \cdot n - p\| \tag{5}$$

$$\text{subject to} \quad n_j \geq 0 \tag{6}$$

The concentration vector $\hat{n}$ solving the program minimizes the norm of the error between the measured value p and the predicted value $\boldsymbol{W} \cdot \hat{n}$. In addition, all components of n must be positive, as a negative particle concentration is unphysical. While this method is simple, it is also vulnerable to noise on the measurements. A more sophisticated reconstruction method such as Tikhonov regularization [29] may be implemented in the future.

IV. Results

A. Calibration

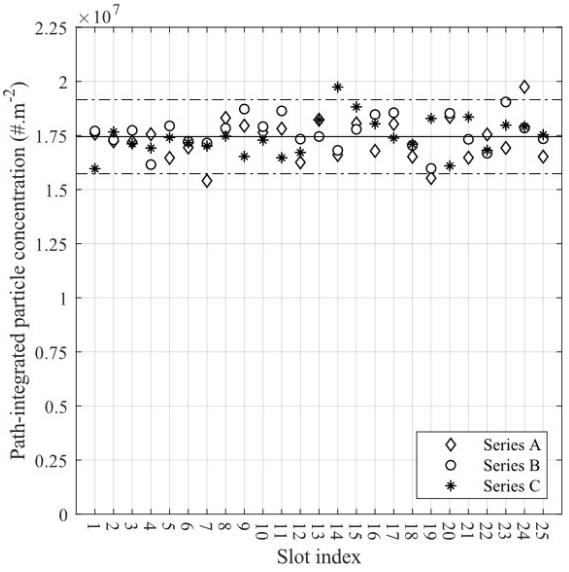

Fig. 8 Path-integrated particle concentration measured by optical counting, organized in slot series A,B and C.

The path-integrated concentration measured through optical counting are presented in Fig. 8. Each slot was measured three times; the results are organized in three series A,B and C of 25 data points covering the entire span of the slot funnel. The results of each series are uncorrelated, which allows us to treat each data point as a single realization of an underlying random variable, regardless of the slot index or series. The mean of the slot concentration is $1.745 \times 10^7 \#.m^{-2}$ with a standard deviation $8.734 \times 10^5 \#.m^{-2}$. Measurement-related errors compound to $4.338 \times 10^5 \#.m^{-2}$ on the result of each slot. The radar measurements for 1 to 25 open slots are presented in Fig. 9 as phase shift plotted against path-integrated concentration. Monte-Carlo simulations are used to derive a 95% confidence interval fit around the Deming regression. The slope of the calibration curve is $\beta_n = (1.379 \pm 0.043) \times 10^{-7}\ ^\circ.\#^{-1}.m^2$. We observe an excellent linearity between phase shift and path-integrated concentration, with a generalized coefficient of determination $r_g^2 = 0.9964$, in agreement with the theoretical model presented in Eq. (1).

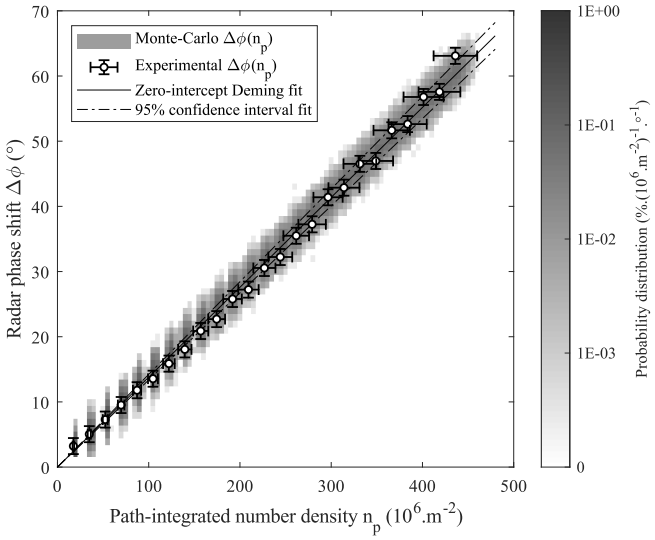

Fig. 9 Radar calibration against path-integrated number concentrations, with Monte-Carlo probability distribution and associated Deming regression slope.

B. Martian and Lunar conditions

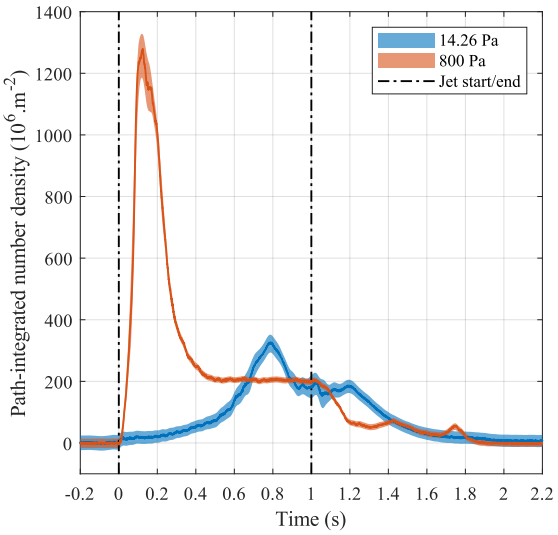

Fig. 10 Path-integrated number concentrations acquired at Martian (800 Pa) and Lunar (14.26 Pa) pressures.

The path-integrated concentrations measured at ambient pressures of 800 Pa (Martian case) and 14.26 Pa (Lunar case) are presented in Fig. 10 with the 95% margin of error shown as the shaded area around the trace. At 800 Pa, we observe that the initial impingement creates a large surge of surface material that reaches a maximum path-integrated concentration of $(1.278 \pm 0.076) \times 10^9$ #.m^{-2} 125 ms after the impact of the jet on the surface. The path-integrated concentration then reaches a steady-state value of $(0.204 \pm 0.010) \times 10^9$ #.m^{-2} that extends between 500 ms and 1021 ms. After 1021 ms, the thruster stops firing, and the concentration decreases, except for two brief surges after the jet is turned off due to the settling of material ejected upward. It is hypothesized that the surge phase is caused by the initial impingement of the jet on the surface. Flat-plate impingement experiment using the same thruster conducted by Al-Rashdan [28] revealed that at the same p_e/p_∞ values encountered in this experiment (2.85 at 800 Pa), a large spike in

ground pressure is observed within the first 20 ms of impingement. The jet is focused and dense, and the absence of a plate shock above the surface in the first milliseconds means that the kinetic energy of the flow has not been converted to internal energy yet. This ensures that most of the flow momentum is transferred to the granular material, liquefying it and generating a large amount of ejecta in a very short time. High-speed footage of the impingement confirms that most of the particles in the surge are lifted in the first 35 ms, with the maximum concentration measured when the particles fall back to the surface [23]. During the steady state, the ejecta cloud is in equilibrium between the particles flux emitted by the crater and the particle flux falling down to the surface. A plate shock has formed above a relatively deep crater, and a combination of bearing capacity failure, diffusion-driven erosion and viscous erosion is lofting particles in the air. The particles follow a ballistic trajectory before falling back to the surface.

At 14.26 Pa, there is no initial surge: the path-integrated concentration shows a sharp but limited increase to $(0.018 \pm 0.025) \times 10^9$ #.m^{-2}, followed by a gradual rise until 787 ms, reaching a peak of $(0.326 \pm 0.025) \times 10^9$ #.m^{-2}. The path-integrated concentration then steadily decreases until 934 ms to reach a value of $(0.175 \pm 0.025) \times 10^9$ #.m^{-2}. It stays somewhat constant until 1197 ms and finally collapses. At this lower pressure, the p_e/p_∞ ratio is initially high (≈ 160), leading to a highly underexpanded jet with a wide cross-section and low density when reaching the surface. No initial ground pressure spike is generated by the jet at Lunar conditions [28], which explains the absence of initial surge. A plate shock appears rapidly and the surface is eroded through viscous processes, as the jet is processed through the shock and deviated from a normal to parallel direction to the surface. However, as the chamber pressure increases during the test, the p_e/p_∞ ratio decreases (≈ 13.4), leading to a denser, more focused jet over time, likely driving the erosion rate up. This could explain why the ejecta concentration does not reach an equilibrium and instead keeps increasing. It is also possible that, as the p_e/p_∞ ratio decreases, the erosion process eventually transitions from viscous erosion to the same erosion modes encountered in Martian conditions, such bearing capacity failure and diffusion-driven erosion. The concentration peak observed at 787 ms followed by a relatively stable concentration at a level close to the one encountered at 800 Pa supports this theory.

The average error on the number concentration is larger at 14.26 Pa than at 800 Pa, 0.023×10^9 #.m^{-2} and 0.017×10^9 #.m^{-2} respectively, despite lower concentrations at 14.26 Pa. This is due to two factors: first, the presence of a significant secondary reflection in the Lunar case, while it is virtually absent in the Martian case. Secondly, vibrations are higher in the Lunar case than in the Martian case, due to the vacuum pumps running continuously to maintain the high vacuum needed, while they are turned off in the Martian case.

C. Altitude-distributed measurements

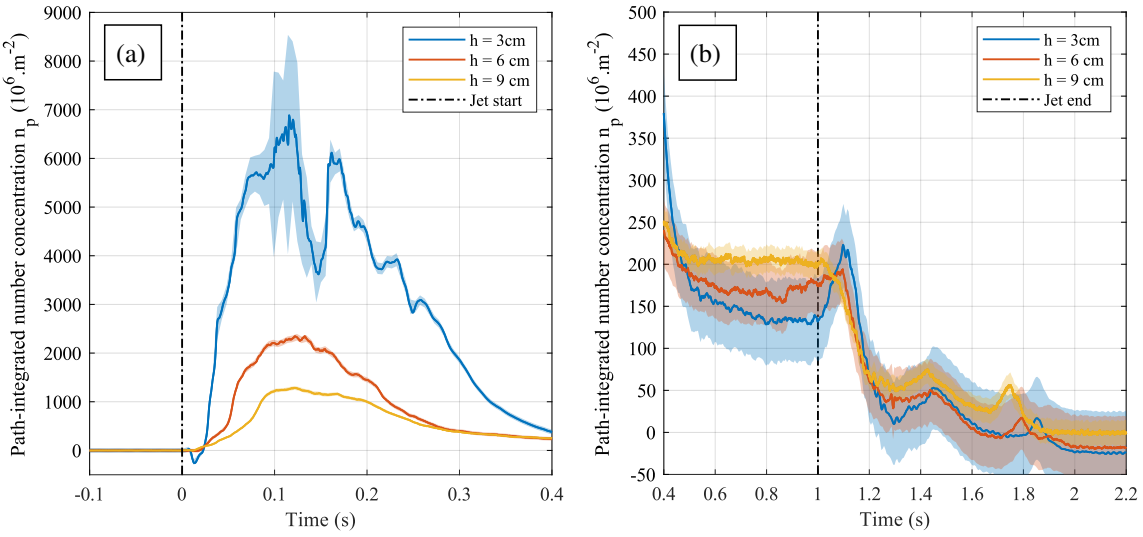

Fig. 11 Path-integrated number concentrations acquired during the initial surge (a), and steady state (b), of the PSI experiment at h/D ratios of 3, 6, and 9 and 800 Pa.

The path-integrated concentrations measured at 3, 6, and 9 cm above the surface are plotted in Fig. 11. Due to the large difference in magnitude in the surge phase and the steady phase, they have been plotted separately in sub-figures (a) and (b), respectively. During the surge phase, the concentration measured by the instrument increases significantly with decreasing altitude. The peak is $(1.284 \pm 0.040) \times 10^9$ #.m^{-2} at 9 cm, $(2.345 \pm 0.051) \times 10^9$ #.m^{-2} at 6 cm, and $(6.881 \pm 1.659) \times 10^9$ #.m^{-2} at 3 cm, a 2 and 5-fold increase respectively. In the steady-state phase, the opposite trend is observed, although the differences are less dramatic. Between 0.5 and 1 s, the average values measured at 3 and 6 cm are (29%) and (16%) lower than the concentration measured at 9cm. A post-jet surge is observed at 3cm, with a peak at $(0.222 \pm 0.050) \times 10^9$ #.m^{-2} (54% higher than the steady-state value) reached 99 ms after jet extinction. The concentration-height relationship in the surge phase can interpreted as the observation of an expanding cloud of particle emitted by a point source, with particle flux following the inverse square law. On the other hand, the inverse trend observed during the steady state is consistent with the equilibrium cloud hypothesized in the previous section: particles are emitted at a given velocity near the surface and follow a near-ballistic trajectory, slowing down - i.e., dwelling longer - at the top of their arc before falling back to the surface.

During the initial surge, we observe that the average error increases when the altitude above the surface decreases, 0.020×10^9 #.m^{-2} at 9 cm, 0.042×10^9 #.m^{-2} at 6 cm, and 0.168×10^9 #.m^{-2} at 3 cm. This is due to extinction by the particles at the higher concentrations encountered close to the surface. The lowest signal-to-noise ratio at 3 cm is on the order of 0.02, against 24 at 6 cm and 42 at 9 cm, leading to a correspondingly large phase error. In the steady-state phase, the error is dominated by secondary reflections, which are significant at 3 and 6 cm: 0.018×10^9 #.m^{-2} and 0.013×10^9 #.m^{-2} respectively, and almost negligible at 9 cm (0.001×10^9 #.m^{-2}).

D. Tomographic measurement demonstration

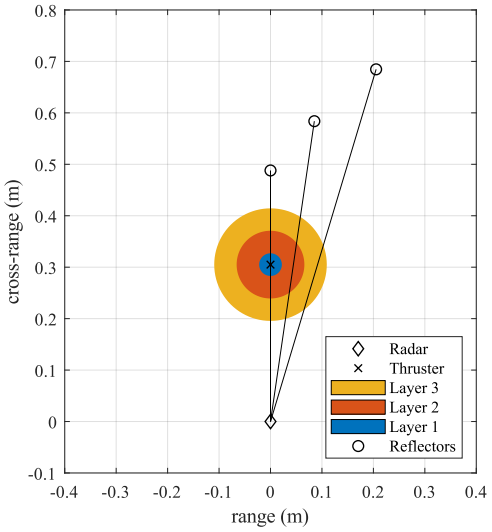

Fig. 12 Configuration of radar and reflectors used in the concurrent measurement experiment, showing the layer structure used for tomographic reconstruction.

The location of the measurements paths used in the experiment and the corresponding regions used in the tomographic reconstruction are plotted, to scale, in Fig. 12. The path-integrated concentration measured by the instrument for each reflector is plotted in Fig. 13, during the surge period (a) and steady-state period (b), with reflector 1 being the innermost and reflector 3 the outermost respectively, as represented in Fig. 5. In the surge phase, the peak on reflector 2 is lower than on reflector 1 and 3. This indicates that layer 2, which is probed most directly through reflector 2, is a low-density region compared to layers 1 and 2. In addition, the path-integrated concentration measured on reflector 1 decreases faster than on reflector 2 and 3, indicating that the high concentration region near the jet core is short-lived compared to the rest of the ejecta cloud. This suggests that particles ejected upward during the initial impact-driven surge will be rapidly cleared by the formation of the aerodynamic structure above the crater. In the steady state regime, the measured concentration is nearly constant across all chords at $\approx 0.200 \times 10^9$ #.m^{-2}. It should be stressed that this does not mean

that the local concentration is uniform across the different layers, since this is a line-integrated measurement.

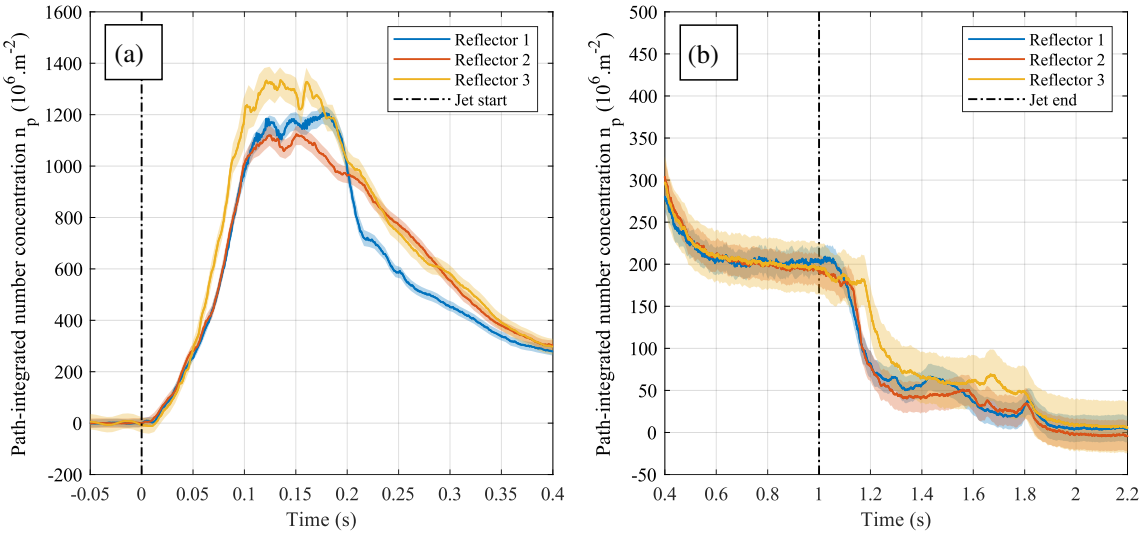

Fig. 13 Path-integrated number concentrations acquired on reflectors 1, 2, and 3 during the initial surge (a), and steady state (b), of the tomographic demonstration experiment at 800 Pa.

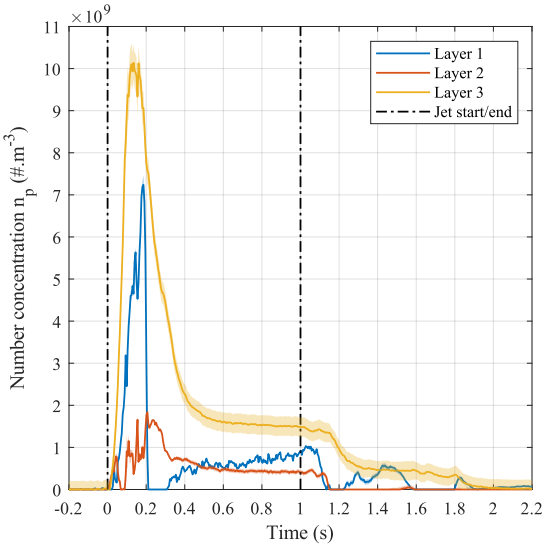

Fig. 14 Number concentrations in layers 1, 2, and 3 derived by tomographic reconstruction.

Tomographic reconstruction of averaged particle number concentration in layers 1 through 3 are shown in Fig. 14. The time traces agree with the observations discussed from the path-integrated results. The outermost layer is the most dense, with peak values of $(10.140 \pm 0.442) \times 10^9$ #.m^{-3}, 1.4 and 5.5 times higher than the maximum values at the core layer 1 and in the intermediate layer 2, respectively. These results suggest that the particle concentration profile along a radii from the axis of the jet presents a valley: there is an intermediary shell of lower number of particles surrounded by higher concentrations near the axis and much higher for the furthest radial positions.

V. Conclusion

Building upon a proof-of-concept system, the improved millimeter-wave radar interferometer has been accurately calibrated, demonstrated in conditions representative of Lunar and Martian landings, and used to measure path-integrated concentrations at various heights and radial positions across the ejecta cloud. The instrument was capable of measuring path-integrated concentration in every configuration tested, including in close proximity to the surface. The calibration of the instrument yielded a phase-ejecta slope $\beta_n = (1.379 \pm 0.043) \times 10^{-7}\ {}^{\circ}.\#^{-1}.m^2$, reducing the measurement uncertainty by an order of magnitude compared to previous calibrations at ambient conditions. The phenomenology of Martian and Lunar ejecta distribution in this study matches the one observed with the previous proof-of-concept. The high linearity and low error of the calibration process, and the replication of the results independently with two different radar systems, verifies the adequacy and robustness of millimeter-wave radar interferometry for high volume loading particle fluid mixtures. Due to its ability to non-intrusively measure time-resolved path-integrated concentrations in optically opaque regimes, millimeter-wave radar interferometry emerges as a unique candidate for future PSI ground tests and even as a flight instrument. The instrument successfully measured path-integrated ejecta concentrations up to $(6.881 \pm 1.659) \times 10^9\ \#.\mathrm{m}^{-2}$ at an altitude of 3 cm and demonstrated that it is inversely correlated with altitude in the initial surge phase and directly correlated with altitude in the steady-state regime. A demonstration of the instrument's tomographic capabilities was conducted. Using 3 reflectors across distributed azimuth and ranges, the concentration of 3 regions located at increasing radial positions from the nozzle axis was measured. While preliminary, those results confirm the feasibility of mmWave interferometric tomography and provide the first experimental insights of particle concentration distributions within ejecta clouds. Future works will expand the tomographic measurement concept by adding more reflectors, radar systems, or even active reflectors, to improve the spatial resolution of the reconstruction, and by enhancing the tomographic reconstruction tools employed. Concurrent particle velocimetry measurements using Doppler-FFT processing and reduced-calibration techniques will also be explored. Overall, the instrument shows high potential, both as a dedicated PSI diagnostic suitable as a flight instrument on a future planetary mission and as a general-purpose diagnostic for a wide variety of opaque, dispersed multiphase flows encountered in aeolian sediment transport, rotorcraft brownouts, and industrial powder processing.

VI. Acknowledgements

This work is supported by the National Aeronautics and Space Administration (NASA) under Grant No. 80NSSC20K0304 issued through the Early Stage Innovation Program. We acknowledge the contributions of Dr. Danehy, NASA Research Collaborator, through fruitful comments and discussions.

References

[1] Drake, B. G., Hoffman, S. J., and Beaty, D. W., "Human exploration of Mars, design reference architecture 5.0," *2010 IEEE Aerospace Conference*, IEEE, 2010, pp. 1–24.

[2] Connolly, J., "Lunar Dust: Lessons from Apollo and a look ahead to Artemis," *The Impact of Lunar Dust on Human Exploration*, 2021, p. 55.

[3] Albee, A., Battel, S., Brace, R., Burdick, G., Casani, J., Lavell, J., Leising, C., MacPherson, D., Burr, P., and Dipprey, D., "Report on the loss of the Mars Polar Lander and Deep Space 2 missions," 2000.

[4] Metzger, P. T., Immer, C. D., Donahue, C. M., Vu, B. T., Latta III, R. C., and Deyo-Svendsen, M., "Jet-induced cratering of a granular surface with application to lunar spaceports," *Journal of Aerospace Engineering*, Vol. 22, No. 1, 2009, pp. 24–32.

[5] Metzger, P., Li, X., Immer, C., and Lane, J., "ISRU Implications for Lunar and Martian Plume Effects," *47th AIAA Aerospace Sciences Meeting including The New Horizons Forum and Aerospace Exposition*, 2009. https://doi.org/10.2514/6.2009-1204, URL http://dx.doi.org/10.2514/6.2009-1204.

[6] Immer, C., Metzger, P., Hintze, P. E., Nick, A., and Horan, R., "Apollo 12 Lunar Module exhaust plume impingement on Lunar Surveyor III," *Icarus*, Vol. 211, No. 2, 2011, pp. 1089–1102. https://doi.org/https://doi.org/10.1016/j.icarus.2010.11.013, URL https://www.sciencedirect.com/science/article/pii/S001910351000432X.

[7] Immer, C., Lane, J., Metzger, P., and Clements, S., "Apollo video photogrammetry estimation of plume impingement effects," *Icarus*, Vol. 214, No. 1, 2011, pp. 46–52. https://doi.org/https://doi.org/10.1016/j.icarus.2011.04.018, URL https://www.sciencedirect.com/science/article/pii/S0019103511001539.

[8] Wagner, S. A., "The Apollo experience lessons learned for constellation lunar dust management," *NASA Technical Publication TP-2006-213726. Washington, DC: National Aeronautics and Space Administration*, 2006.

[9] Munk, M. M., "Aerocapture, Entry Descent and Landing (AEDL) Overview," *19th International Planetary Probe Workshop (IPPW)*, 2020.

[10] Vizcaino, J., and Mehta, M., "Quantification of plume-soil interaction and excavation due to the Mars Science Laboratory Sky Crane Descent Phase," *8th Symposium on Space Resource Utilization*, 2015. https://doi.org/10.2514/6.2015-1649, URL https://arc.aiaa.org/doi/abs/10.2514/6.2015-1649.

[11] You, J., Zhang, X., Zhang, H., Li, C., Xu, Y., Yan, Q., Yu, H., Liu, J., Li, Y., Wang, Y., et al., "Analysis of plume–lunar surface interaction and soil erosion during the Chang'E-4 landing process," *Acta Astronautica*, Vol. 185, 2021, pp. 337–351.

[12] Tyrrell, O. K., Thompson, R. J., Danehy, P. M., Dupuis, C. J., Munk, M. M., Nguyen, C. P., Maddock, R. W., Fahringer, T. W., Krolick, W. C., Weaver, A., et al., "Design of a lunar plume-surface interaction measurement system," *AIAA SCITECH 2022 Forum*, 2022, p. 1693.

[13] White, C., Zare-Behtash, H., Kontis, K., Ukai, T., Merrifield, J., Evans, D., Coxhill, I., Langener, T., and Van den Eynde, J., "Test Facility to Investigate Plume-Regolith Interactions," 2019.

[14] Eberhart, C. J., West, J., and Korzun, A. M., "Overview of Plume-Surface Interaction Data from Subscale Inert Gas Testing at NASA MSFC Test Stand 300 Vacuum Facilities," *AIAA SCITECH 2022 Forum*, AIAA, 2022. https://doi.org/10.2514/6.2022-1811, URL https://arc.aiaa.org/doi/abs/10.2514/6.2022-1811.

[15] Diaz-Lopez, M. X., Gorman, M., Rubio, J. S., and Ni, R., "Plume-surface Interaction Physics Focused Ground Test 1: Diagnostics and Preliminary Results," *AIAA SCITECH 2022 Forum*, AIAA, 2022. https://doi.org/10.2514/6.2022-1810, URL https://arc.aiaa.org/doi/abs/10.2514/6.2022-1810.

[16] Rubio, J. S., Gorman, M., Diaz-Lopez, M. X., and Ni, R., "Plume-Surface Interaction Physics Focused Ground Test 1: Setup and Preliminary Results," *AIAA SCITECH 2022 Forum*, 2022. https://doi.org/10.2514/6.2022-1809, URL https://arc.aiaa.org/doi/abs/10.2514/6.2022-1809.

[17] Metzger, P. T., Latta, R. C., Schuler, J. M., and Immer, C. D., "Craters Formed in Granular Beds by Impinging Jets of Gas," *AIP Conference Proceedings*, Vol. 1145, No. 1, 2009, pp. 767–770. https://doi.org/10.1063/1.3180041, URL https://aip.scitation.org/doi/abs/10.1063/1.3180041.

[18] Metzger, P. T., "Rocket Exhaust Blowing Soil in Near Vacuum Conditions Is Faster than Predicted by Continuum Scaling Laws," *Earth and Space 2016*, 2016, pp. 58–66. https://doi.org/10.1061/9780784479971.007, URL https://ascelibrary.org/doi/abs/10.1061/9780784479971.007.

[19] Watkins, R., Metzger, P., Mehta, M., Han, D., Prem, P., Sibille, L., Dove, A., Jolliff, B., Moriarty, D., Barker, D., Patrick, E., Kuhns, M., Laine, M., and Radley, C., "Understanding and Mitigating Plume Effects During Powered Descents on the Moon and Mars," *Bulletin of the AAS*, Vol. 53, No. 4, 2021. https://doi.org/10.3847/25c2cfeb.f9243994, URL https://baas.aas.org/pub/2021n4i089.

[20] Lane, J. E., and Metzger, P. T., "Estimation of Apollo Lunar Dust Transport using Optical Extinction Measurements," *Acta Geophysica*, Vol. 63, No. 2, 2015, pp. 568–599. https://doi.org/10.1515/acgeo-2015-0005, URL https://doi.org/10.1515/acgeo-2015-0005.

[21] Lane, J. E., Mantovani, J. G., Mueller, R. P., Nugent, M. W., Nick, A. J., Schuler, J. M., and Townsend, I. I., "Optical Extinction Measurements of Dust Density in the GMRO Regolith Test Bin," *Earth and Space 2016*, 2016, pp. 36–47. https://doi.org/10.1061/9780784479971.005, URL https://ascelibrary.org/doi/abs/10.1061/9780784479971.005.

[22] Metzger, P. T., Dove, A., Conroy, M., Gloria, J., O'Reilly, A., and St. John, A., "Ejecta Sheet Tracking, Opacity, and Regolith Maturity (Ejecta Storm): An Instrument for Lunar Landing Plume Effects and Dust Dynamics," *Lunar and Planetary Science Conference*, 2021, p. 2616.

[23] Rasmont, N., Al-Rashdan, H. T., Elliott, G., Rovey, J., and Roca, L. V., "Millimeter Wave Interferometry for Ejecta Concentration Measurements in Plume-Surface Interactions," *AIAA SCITECH 2022 Forum*, AIAA, 2020. https://doi.org/10.2514/6.2022-2421, URL https://arc.aiaa.org/doi/abs/10.2514/6.2022-2421.

[24] Markel, V. A., "Introduction to the Maxwell Garnett approximation: tutorial," *Journal of the Optical Society of America A*, Vol. 33, No. 7, 2016, pp. 1244–1256. https://doi.org/10.1364/JOSAA.33.001244, URL http://josaa.osa.org/abstract.cfm?URI=josaa-33-7-1244.

[25] *IWR1443BOOST*, Texas Instruments, 2020. URL https://www.ti.com/lit/ug/swru518d/swru518d.pdf, rev. D.

[26] *DCA1000EVM Data Capture Card*, Texas Instruments, 2018. URL https://www.ti.com/lit/ug/spruij4a/spruij4a.pdf, rev. A.

[27] Rodríguez, J. M., Hristov, H. D., and Grote, W., "Fresnel zone plate and ordinary lens antennas: Comparative study at microwave and terahertz frequencies," *2011 41st European Microwave Conference*, 2011, pp. 894–897.

[28] Al-Rashdan, H., "Supersonic Underexpanded Flow Visualization in Sub-Atmospheric Facility," *AIAA AVIATION 2021 FORUM*, AIAA, 2021. https://doi.org/10.2514/6.2021-2859, URL https://arc.aiaa.org/doi/abs/10.2514/6.2021-2859.

[29] Och, A., Hölzl, P. A., Schuster, S., Scheiblhofer, S., Zankl, D., Pathuri-Bhuvana, V., and Weigel, R., "High-Resolution Millimeter-Wave Tomography System for Nondestructive Testing of Low-Permittivity Materials," *IEEE Transactions on Microwave Theory and Techniques*, Vol. 69, No. 1, 2021, pp. 1105–1113. https://doi.org/10.1109/TMTT.2020.3030662.